

不可逆; 单向的, 非交互的, 非互易的



Inverse-designed non-reciprocal pulse router for chip-based LiDAR

Ki Youl Yang^{1,7}, Jinhie Skarda^{1,7}, Michele Cotrufo^{2,3,7}, Avik Dutt¹, Geun Ho Ahn¹, Mahmoud Sawaby^{1,4}, Dries Vercruyse¹, Amin Arbabian^{1,4}, Shanhui Fan¹, Andrea Alù^{1,2,3,5,6} and Jelena Vučković¹✉

Non-reciprocal devices such as isolators and circulators are key enabling technologies for communication systems, both at microwave and optical frequencies. Although non-reciprocal devices based on magnetic effects are available for free-space and fibre-optic communication systems, their on-chip integration has been challenging, primarily due to the concomitant high insertion loss, weak magneto-optical effects and material incompatibility. We show that $\chi^{(3)}$ nonlinear resonators can be used to achieve all-passive, low-loss, bias-free non-reciprocal transmission for applications in photonic systems such as chip-scale LiDAR. A multi-port nonlinear Fano resonator is used as an on-chip, non-reciprocal pulse router for frequency comb-based optical ranging. Because time-reversal symmetry imposes stringent limitations on the operating power range and transmission of a single nonlinear resonator, we implement a cascaded Fano-Lorentzian resonator system that overcomes these limitations and substantially improves the insertion loss and operating power range of current state-of-the-art devices. This work provides a platform-independent design for non-reciprocal transmission and routing that is ideally suited for photonic integration.

Non-reciprocal devices have become key components for enabling transmission and reception on the same communication channel, contributing to the rise of the new generation of cellular networks (5G) based on full-duplex radiofrequency communications. Similarly, as optical-frequency systems advance, it is becoming increasingly important to implement non-reciprocal devices in silicon photonic circuits. The ability to miniaturize non-reciprocal systems towards the portable mobile scale and boost their performance is enabling a wide range of applications in optical communications, signal processing, spectroscopy and sensing. So far, integrated non-reciprocal devices have been demonstrated by using spatiotemporal modulation^{1–3}, magnetic bias^{4–6}, Brillouin scattering^{7,8} and optical nonlinearities^{9–15}. Although it is well established that in a linear material non-reciprocity requires an external bias that breaks time-reversal symmetry, $\chi^{(3)}$ nonlinear devices eliminate this need and can be implemented in a monolithically integrated platform. Such devices can thus greatly simplify the fabrication steps as well as device design and operation. Despite the constraints imposed by dynamic reciprocity¹⁶ on passive nonlinear devices under simultaneous excitation from both ports, silicon $\chi^{(3)}$ nonlinear devices are still attractive if the outstanding challenges of integrated non-reciprocal devices¹⁷ can be overcome. In particular, optical isolation in large-scale integrated photonics has remained elusive, mainly due to issues with high insertion loss^{2–6,10,17,18}, narrow bandwidth¹⁹ and scalability^{5,8}. The development of such a silicon-based chip-scale non-reciprocal device may lead to novel nonlinear devices and systems for applications in optical communications and LiDAR (light detection and ranging)²⁰.

Here, we demonstrate all-passive, bias-free non-reciprocal transmission and routing of mode-locked pulse streams in silicon

photonic systems. First, an asymmetric Fano resonator is implemented with a conventional microresonator side-coupled to a bus waveguide containing compact inverse-designed reflectors. $\chi^{(3)}$ nonlinearity enables self-biased and high-speed non-reciprocal transmission in the silicon microresonators, and our device exhibits record-low insertion loss and a high non-reciprocal transmission ratio. Addition of a drop waveguide to the silicon Fano resonator enables non-reciprocal routing of a pulsed signal, and we demonstrate its usefulness for frequency comb-based optical ranging. In particular, we experimentally demonstrate a chip-based LiDAR system, which enables distance measurements at up to 60 m with a bias-free, fully passive non-reciprocal device. Importantly, it has been recently shown that any nonlinear single-resonator device is affected by a fundamental tradeoff²¹ between the maximum forward transmission (T) and the range of powers over which non-reciprocal transmission can occur—typically termed the non-reciprocal intensity range (NRIR)—given by

$$T \leq \frac{4 \times \text{NRIR}}{(\text{NRIR} + 1)^2} \quad (1)$$

Therefore, a larger T can be obtained only at the expenses of a smaller NRIR, and vice versa²¹. By characterizing several single-resonator devices we provide experimental and systematic verification of this bound. For practical photonic applications it is extremely important to relax this tradeoff between operating power range and transmission¹⁷. As recently shown²², the single-resonator bound can be overcome by cascading two nonlinear resonators. Following this approach, we exploit the large versatility of our inverse design and fabrication process to implement a cascaded Fano–Lorentzian

¹E. L. Ginzton Laboratory, Stanford University, Stanford, CA, USA. ²Photonics Initiative, Advanced Science Research Center, City University of New York, New York, NY, USA. ³Department of Electrical and Computer Engineering, The University of Texas at Austin, Austin, TX, USA. ⁴Department of Electrical Engineering, Stanford University, Stanford, CA, USA. ⁵Physics Program, Graduate Center, City University of New York, New York, NY, USA. ⁶Department of Electrical Engineering, City University of New York, New York, NY, USA. ⁷These authors contributed equally: Ki Youl Yang, Jinhie Skarda, Michele Cotrufo. [✉]e-mail: jela@stanford.edu

resonators device. This allows us to obtain near-unity transmission ($T > 98\%$) for NRIR > 6 dB, largely beating the single-resonator bound. Beyond the direct demonstration and application of these nonlinear non-reciprocal devices, this work illustrates a platform-independent design method to unlock novel functionalities in integrated nonlinear optics such as saturable absorption and nonlinear signal processing.

Results

Device implementation. The mechanism exploited here to achieve passive non-reciprocity relies on a combination of geometrical asymmetry and electromagnetic nonlinearity. When an asymmetric two-port resonator is optically pumped from one of the two ports, different intracavity intensities are obtained depending on the input port chosen. A $\chi^{(3)}$ nonlinearity inside the resonator will therefore lead to a different cavity frequency shift for the same input power. This mechanism can enable efficient and low-power non-reciprocal transmission if the induced frequency shift is comparable to the detuning between the points of maximum and minimum transmission of the linear device. A sharp frequency response can be obtained by engineering a Fano resonance, where the interference between discrete cavity resonances and the continuum of waveguide modes creates an asymmetric lineshape with a sharp transition between transmission dips and peaks^{21,22}. The forward transmission in this single-resonator scheme is constrained to follow the fundamental bound imposed by equation (1) and is further limited by any additional intrinsic loss mechanism. Cavities with low intrinsic loss can thus allow device operation very close to the fundamental bound when properly optimized.

We implemented the two-port Fano resonance device with a high-Q (quality factor) silicon racetrack resonator coupled to a silicon bus waveguide containing an inverse-designed reflector, as illustrated in Fig. 1a. The device layer has a thickness of 220 nm on 2 μm -thick silicon oxide layer, and the resonator was designed to operate in single mode at a wavelength of 1,550 nm (Fig. 1a, inset 2). Using fabrication-constrained inverse design^{23,24}, a partially transmitting element (PTE) was designed in the waveguide at the resonator coupling region to create a Fano lineshape in the cavity response function^{25–28}. It is important to note that intrinsic cavity loss can be seriously degraded due to parasitic loss of the PTE^{12,28}, but, inverse design enables us to mitigate additional cavity loss through the PTE while managing the cavity-waveguide coupling strength in parallel (Supplementary Sections III and IV). Moreover, the low intrinsic loss of the resonators allows relatively small resonator-waveguide coupling to be the dominant cavity loss, enabling these single-resonator devices to operate near the fundamental bound and achieve almost the maximum forward transmission constrained by a given non-reciprocal intensity range. Although operating in this over-coupled regime reduces the loaded cavity Q and hence reduces the resonant power enhancement, the sharp lineshape featured by Fano resonators as well as the low intrinsic loss can still provide non-reciprocal transmission at moderate power levels^{21,22}.

The PTE is positioned with a slight offset (for more details see Methods) from the centre of the coupling region toward the input port, so as to create asymmetric coupling to the resonator from opposite ports¹². For the specific device shown in Fig. 1, we designed the PTE to provide a reflection of 80%. As explained in refs. ^{21,22,29}, reflection at the input port is required for the device to support an asymmetry between the strength of the resonator coupling at the two ports, which in turn controls the maximum achievable NRIR²¹; for the chosen reflectivity level of 80%, the NRIR of the device can be as large as 9 dB (see Supplementary Section III for details). Inset 4 in Fig. 1a shows the inverse design optimization trajectory and a scanning electron micrograph (SEM) image of the fabricated PTE structure. Spectral measurements of a single microresonator with the PTE were performed by monitoring the waveguide transmission

as the laser wavelength was scanned, and the right panel of inset 4 presents a spectral scan near 1,541.5 nm. Linewidth extracted from the fitted Fano curve²⁵, shown in red, gives a loaded Q factor of 1.4×10^4 , an unloaded Q factor of 8.9×10^4 and a non-resonant reflection of 81.6%.

Device characterization. To validate the operation of the Fano non-reciprocal device, we measured the forward and backward transmission over a 12 dB range of continuous-wave (c.w.) input (Fig. 1b). Following previous works,^{21,22} we define the NRIR as the ratio of input powers from opposite propagation directions that leads to the threshold-like transmission transition. The forward and backward transmissions were measured without counter-propagating waves (for more experimental details see Methods). The maximum transmission contrast between the two directions is 20.3 dB (minimum of 12.9 dB) and the average contrast is 17.7 dB within the operating power range indicated by the shaded region. The maximum forward transmission is 77% (corresponding to an insertion loss of 1.1 dB) and the non-reciprocal operation range is 4.5 dB (operation power of 4.55–9.05 dBm loaded on the silicon waveguide). We note that the non-reciprocal device performance falls within the bound in equation (1), as the maximum forward transmission allowed with this NRIR is 80%. We have experimentally verified that this bound holds for many other single-resonator devices, as shown later in Fig. 3b. Importantly, our device design enables the implementation of single Fano cavities that operate close to the bound and thus achieves insertion loss lower than the record values of current state-of-the-art devices (Supplementary Section VIII)^{2,6,10,12,18}.

To demonstrate the applicability of this Fano non-reciprocal device to high-speed signal processing, we also characterize the forward and backward transmission with a 10 GHz modulated c.w. signal (Fig. 1c) generated using a Mach-Zehnder (MZ) modulator¹². We use a peak power of ~ 5 mW (~ 7 dBm), corresponding to an average energy of ~ 250 fJ per period. The forward transmission follows the input sinusoidal waveform with ~ -15 dB of total harmonic distortion and -1.05 dB average insertion loss, while the backward transmission is strongly suppressed. The transmission trace is naturally compressed at low input powers due to the threshold-like transfer function (Fig. 1b). The non-reciprocal transmission ratio and NRIR decrease as the modulation frequency increases (Supplementary Section VII), but we did not observe insertion loss change within our experimental bandwidth (0–15 GHz), and the distortion due to finite bandwidth can be mitigated by using a resonator with lower Q (obtained by increasing the waveguide-ring coupling), while the consequential increase of the operating power can be mitigated by reducing the mode volume (Supplementary Section III). The operation of the particular device shown in Fig. 1 is limited to pulse widths greater than 100 ps, set by the cavity decay rate, and a detailed characterization is provided in Supplementary Section III. The threshold-like input–output power transfer function and high-speed operation capability, demonstrated in Fig. 1b,c, satisfy requirements for an all-optical regenerator^{30–32} and point to its potential usefulness not only for non-reciprocal devices but also for nonlinear signal processing in optical communications.

Demonstration of optical ranging measurement based on non-reciprocal transmission and all-optical routing. Although $\chi^{(3)}$ -based non-reciprocal devices are fundamentally limited by time-reversal symmetry and thermodynamic considerations, their passive, magnet-free, bias-free, simple architecture makes them particularly appealing for integrated photonics. We show how these devices can be used in a range of important photonic systems operating with pulsed signals, where the forward and backward ports are not simultaneously excited (Supplementary Fig. 7). Despite recent advances in photonic integration, such as large-scale phased array³³

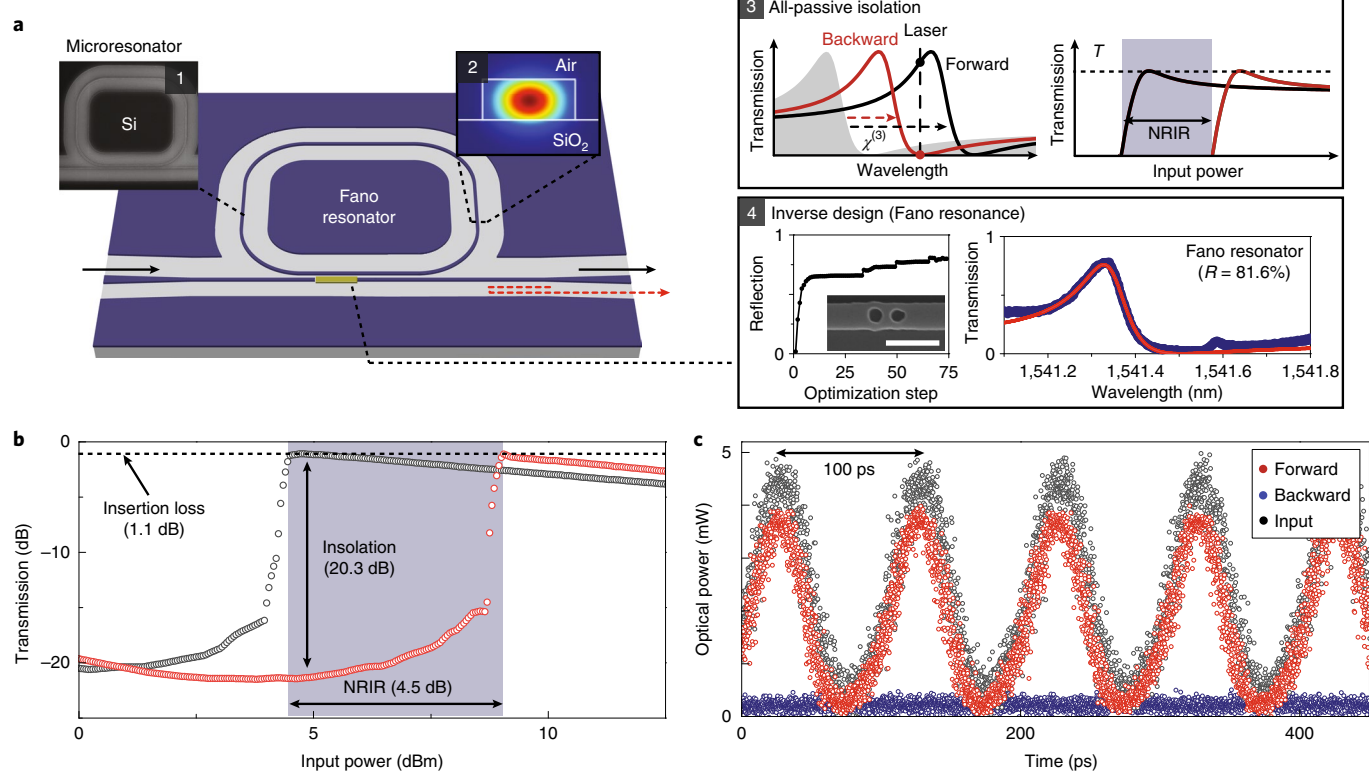


Fig. 1 | All-passive non-reciprocal transmission using a silicon photonic resonator. **a**, Schematic of the Fano non-reciprocal device. The silicon resonator (inset 1: SEM image of the resonator) only supports a fundamental transverse-electric (TE) mode (inset 2: simulated spatial mode profile). A silicon waveguide is side-coupled to the racetrack resonator, and the yellow box on the waveguide shows the location of the inverse-designed reflector used to synthesize Fano resonances. This inverse design area is offset with respect to the centre of the cavity-waveguide coupling region to break the symmetry between the forward- and backward-direction coupling rates. As a result, forward- and backward-direction excitation with the same input intensity produces different shifts of the resonator resonant frequency, and thus of the transmission lineshape (inset 3). In inset 4, the left plot presents the inverse design optimization trajectory, showing the simulated device reflection versus optimization iteration, as well as an SEM image of the final fabricated inverse-designed reflector (scale bar, 1 μm). The right plot presents the measured transmission spectrum of the fundamental TE mode in the silicon racetrack resonator with the inverse design reflector. Red line is a fit of the data with a Fano model. **b**, Measured transmission versus input power to the Fano resonator in the forward (black) and backward (red) directions. The c.w. input is coupled to the input and output ports separately, and the transmitted signal is measured at the opposite port. **c**, Transmitted signal trace of a 10 GHz modulated c.w. signal for excitation in either the forward or backward propagation directions (monitored by a digital communication analyser). The measured output power is calibrated with the chip-to-fibre interface efficiency. Note that the input optical signal has distortion due to the nonlinear response of the Mach-Zehnder interferometer-based intensity modulator and radiofrequency amplifier used to generate the signal (Supplementary Section VII).

and microcomb sources²⁰, which are a promising step towards miniaturization of LiDAR systems, other chip-based components like isolators and circulators are still required in a full system to harness the potential of these approaches. As a demonstration of how our silicon device is useful for integrated LiDAR systems, we performed precise and reliable optical distance measurements using a frequency comb as the source and our device as both the on-chip non-reciprocal transmitter and router. A pulse routing waveguide was added to the Fano non-reciprocal device (see device schematic in Fig. 2a) to enable the device to guide the pulses from both the pump laser and the detection target to the same photodetector while protecting the pump laser from the reflected pulse.

The experimental schematic used for the optical ranging measurement is illustrated in Fig. 2a. For mode-locked pulse generation, we use a fibre ring resonator consisting of an erbium-doped fibre amplifier, a semiconductor optical amplifier, polarization controller and bandpass filter. The 5 MHz pulse repetition rate allows measuring distances up to 60 m, and the central frequency of the pulse can be adjusted to the Fano device operation range using the bandpass filter. The generated pulse streams are split by a 50:50 fibre-based coupler and one part is directly sent to device port 1. The other part

of the pulse stream is first passed through a fibre delay line (physical path length ~5, 20, 25, 30 m) and then sent to port 2. The pulse stream coupled to port 2 does not propagate to port 1 because of the Fano resonator (as checked by monitoring PD1, Fig. 2c), while the pulse stream from port 1 is transmitted to port 2 of the device (monitored at PD2). The device routes the pulse stream from port 2 to port 3 in the other waveguide coupled to the Fano resonator (Fig. 2b), where it combines with the input pulse stream from port 1 to generate an electric signal trace of dual pulse streams (Fig. 2d) at PD3. An enlarged view of the trace (lower panel, Fig. 2d) shows the reference and target peaks within two periods of 192 ns, and the time interval between reference and target peaks is calculated for each period and converted to the distance scale. Figure 2e plots distance versus time, where the time increment is the reference pulse period, showing the stability of the distance measurement. To extend this distance measurement set-up into a LiDAR system, the device can be equipped with an integrated microlens^{20,34}, metasurface³⁵ and phased array³³ at port 2 to emit the pulse stream from port 1 towards the target and to receive the reflected pulse streams. The received pulse in a typical LiDAR system is a low-intensity signal, so back-reflection at the isolated port and pulse emitter of the signal

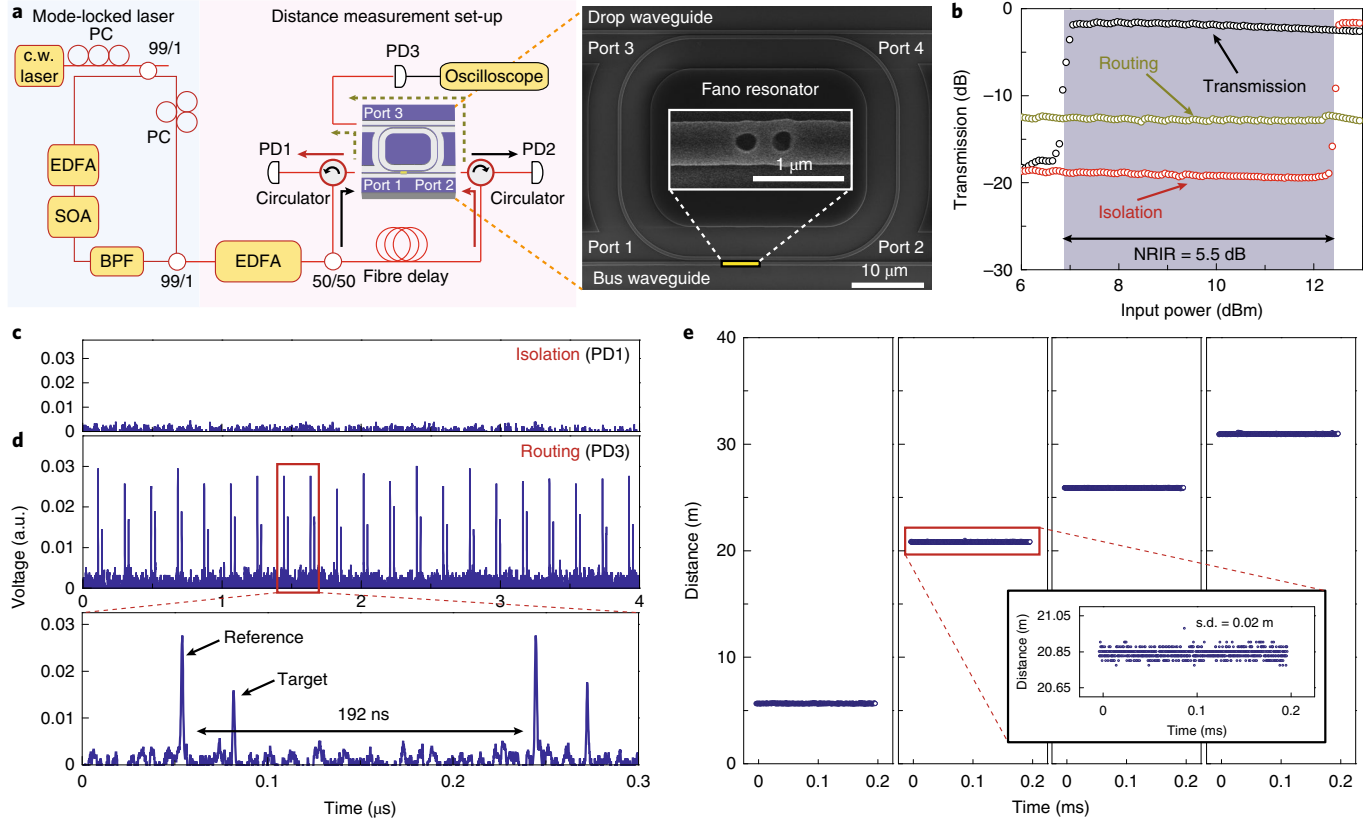


Fig. 2 | Non-reciprocal pulse routing and optical distance measurement. **a**, Schematic of the pulsed laser generation set-up (left) and optical distance measurement set-up (right). A c.w. laser is polarization controlled (polarization controller, PC) and split using a 99/1 coupler to pump the fibre loop resonator. An erbium-doped fibre amplifier (EDFA) and a semiconductor optical amplifier (SOA) are used as the gain media of the fibre laser⁴⁴, and a bandpass filter (BPF) selects the central frequency of the output pulse. For the distance measurements, the pulse stream is split into two paths: the reference path is directly connected to device port 1, while the target path includes a fibre delay before port 2. The pulse streams of both paths are routed to port 3 and detected at photodetector 3 (PD3) for time-of-flight measurements. PD2 monitors the forward transmission through the device. PD1 records the transmission of the target path pulse stream from port 2 to port 1, thus monitoring the device's ability to isolate the pulsed laser input source. Inset: SEM image of the device. **b**, Transmission versus input power for a c.w. input through three different propagation paths corresponding to transmission (S_{12}), isolation (S_{21}) and routing (S_{22}), where S_{ij} indicates transmission from port i to port j . **c**, The electrical intensity trace of PD1 during optical ranging, demonstrating isolation of the pulsed laser input source. **d**, Representative electrical intensity trace from PD3 showing reference and target pulses containing ranging information. The lower panel presents an enlarged view of the electrical intensity trace over two pulse periods. The pulse period is ~192 ns. **e**, The measured distance between the reference peak and target peak versus time (data acquisition time, 200 μs) for fibre delay path lengths of 5, 20, 25 and 30 m, respectively (left to right). Inset: enlarged view of the measured distance trace showing a s.d. of 0.02 m, demonstrating the stability of this optical distance measurement. The range ambiguity in this measurement is ~40 m in silica fibre.

is also weak, making it practically suitable for a precise distance measurement. Our Fano non-reciprocal transmitter-router device can protect the pulsed laser source from the reflected pulse streams for stable system operation while routing light from these reflected pulses to the other waveguide. In this measurement, the reference and reflected pulses do not arrive on our device at the same time and hence bypass the dynamic non-reciprocity constraint¹⁶. Such operation, in principle, can also be realized using active time-gated switching, but high-speed operation is challenging³⁶. Furthermore, we expect that the reflected pulses can be isolated even under simultaneous excitation if another Fano resonator is connected in series with a time delay corresponding to half the pulse width (Supplementary Section VI). Based on these findings, our experiment demonstrates the viability of the realized passive non-reciprocal transmitter and router to act as an essential component in a fully integrated chip-scale LiDAR system.

Operation over a broad power range based on cascaded nonlinear resonances. Unlike linear non-reciprocal devices that can

potentially work under any input power, nonlinear passive devices based on a single resonator can lead to non-reciprocal transmission only over a limited range of signal powers (NRIR). In fact, as already mentioned above, single-resonator devices are affected by a fundamental tradeoff between the maximum achievable forward transmission and the NRIR²¹. Here, we provide the first experimental verification of this fundamental constraint by characterizing several single-resonator devices. The different designs are obtained by varying the reflectivity of the inverse-designed coupling element and the cavity-waveguide gaps in the device in Fig. 1a. The blue bars in Fig. 3b show the measured forward transmissions and NRIRs for each single-resonator device, and the shaded region corresponds to the theoretical bound in equation (1). For each device, the two edges of the corresponding bar in Fig. 3b denote the minimum and maximum transmission within the NRIR. All the investigated single-resonator devices are clearly constrained by the bound. As an example, panels 1 and 2 of Fig. 3c show transmission versus input power for single resonators in the forward and backward directions. These results clearly illustrate that a highly transmissive ($T=0.96$) device

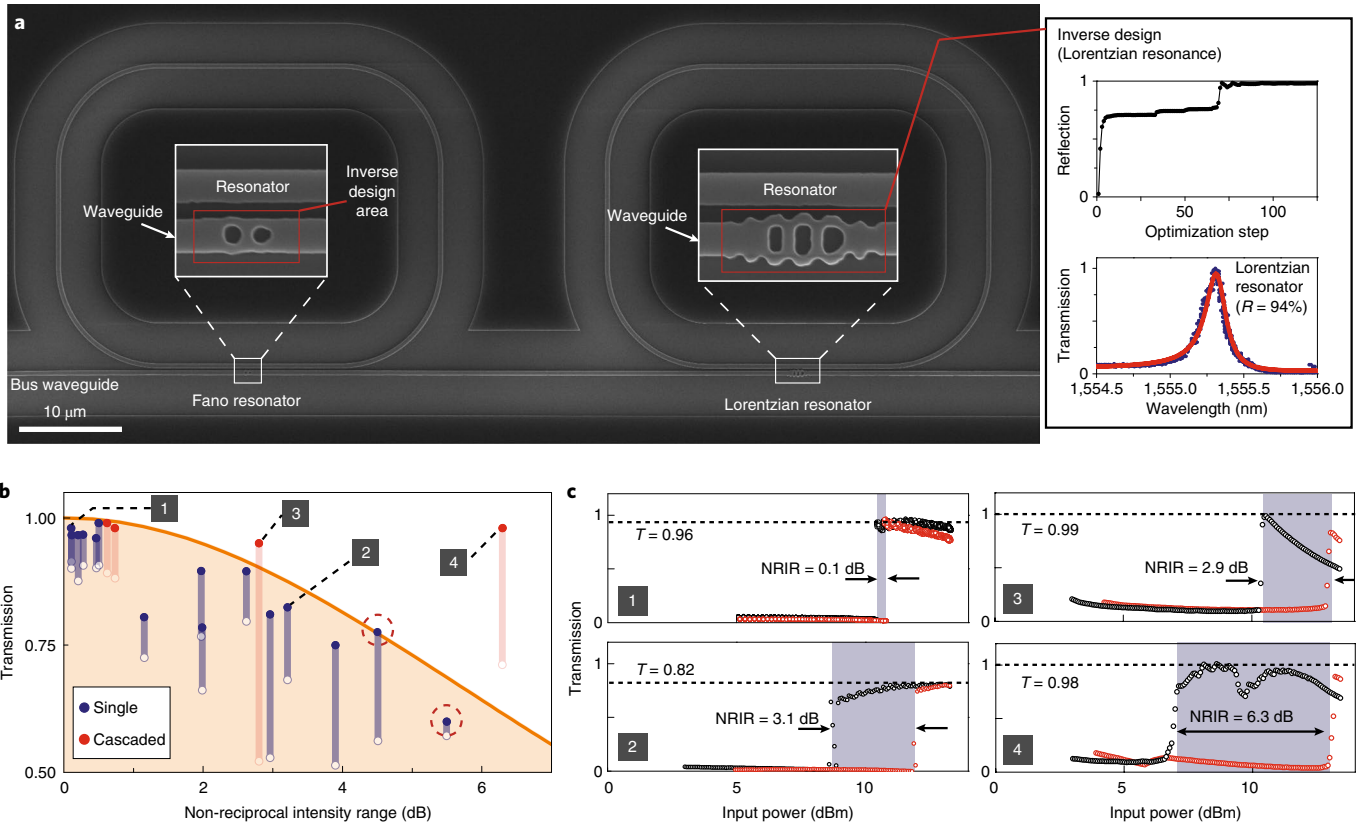


Fig. 3 | Non-reciprocal transmission in broad operating power range using cascaded nonlinear resonators. **a**, SEM image of cascaded Fano-Lorentzian resonators implemented on a silicon-on-insulator platform. The enlarged images show inverse-designed reflectors on the silicon waveguide in the resonator-waveguide coupling region. Inset: the inverse design of the $R = 94\%$ reflector used to implement a Lorentzian resonator (top: optimization trajectory to obtain the desired non-resonant high reflection; bottom: low-power transmission of a single device with non-resonant reflection $R = 94\%$, red line is a fit with a Lorentzian lineshape). The Fano resonator is implemented using the same inverse-designed reflector shown in the inset of Fig. 1a. **b**, Forward transmission (filled and open circles indicate maximum and minimum transmission, respectively, within the operating power range) versus non-reciprocal intensity range for single (blue) and cascaded (red) resonators. The shaded region corresponds to the theoretical bound on single resonator operation^{21,22} and bars represent the range of transmission within NRIR. The dots outlined with red-dashed circles are measurement results for the devices presented in Figs. 1 and 2. **c**, Measured transmission versus input power of single resonators (1 and 2) and cascaded resonators (3 and 4) in the forward (red) and backward (black) directions.

is affected by a narrow operating power range (~ 0.1 dB), while a less transmissive ($T=0.82$) device can operate over a broader power range (3.1 dB). If unitary transmission is required, the operation range for a single resonator device shrinks to zero.

Increasing the operating power range of these devices while keeping quasi-unitary transmittance is fundamental for their use in many photonic applications¹⁷. It was shown in ref. ²² that two cascaded nonlinear resonators, interleaved by properly chosen delay lines, can overcome this constraint and realize non-reciprocal transmission over a broad operating power range, beyond the bound in equation (1). We implemented the system proposed in ref. ²², consisting of cascaded Fano–Lorentzian resonators (Fig. 3a). The Lorentzian response is obtained using the same waveguide-coupled racetrack resonator configuration, but with a highly reflective coupling element obtained again by inverse design (right inset, Fig. 3a). The Fano resonator is similar to the device characterized in panels 1 and 2 of Fig. 3c, but with a coupler element designed to obtain 56% reflectance. A key element to overcome the single-resonator bound is the ability to control the phase delay between the Fano and Lorentzian resonators²². In our device, the phase delay is set lithographically by the physical length between the two reflector elements along the waveguide. We characterized several Fano–Lorentzian cascaded systems, with various phase delays, and compared their operations with the single Fano devices. The red bars in Fig. 3b

show the transmission versus NRIR of four cascaded resonators measured at the same wavelength as the single-resonator systems. For selected phase delays we obtain a clear breaking of the single-resonator bound (panels 3 and 4 of Fig. 3c, and bars labelled ‘3’ and ‘4’ in Fig. 3b). For the device shown in Fig. 3c, panel 4, a maximum forward transmission of 98% (0.17 dB insertion loss) is achieved while maintaining at the same time an NRIR (6.3 dB) much bigger than the one allowed by the single resonator limit (compare with Fig. 3b). We note that the forward transmission fluctuates within the NRIR. This is because the transmitted power is controlled by the total phase (ϕ) accumulated by the laser beam during a roundtrip, which depends, among other parameters, on the detuning between the laser and resonator frequencies. The cavity frequencies, in turn, depend on the intracavity intensities due to the $\chi^{(3)}$ nonlinearity, thus introducing a nontrivial dependence of ϕ on the input power (for further discussion see Supplementary Information). It is worth noting that, despite these transmission fluctuations, the two-resonator cascaded devices can still be designed to break the single-resonator bound for any value of power within the NRIR. For the device shown in Fig. 3c, panel 4, for example, the minimum forward transmission within the NRIR is $\sim 71\%$. This value, although smaller than the maximum (98%), still breaks the single-resonator bound (compare with Fig. 3b for an NRIR of 6.3 dB). We note that, in this all-passive device experiment, no attempt to actively control

the resonance wavelengths and phase delay was made, but, in the future, thermo- or electro-optic control can be introduced to further optimize the performance. These experimental results demonstrate a practical and feasible solution to overcome the power range constraints of nonlinear devices. In addition, the capability to precisely tailor the coupling between nonlinear resonators and a common reservoir could allow, for example, the realization of arrays of nonlinear elements with self-induced topological protection in the optical domain³⁷.

Conclusion

In summary, we have demonstrated that $\chi^{(3)}$ nonlinear resonators can be used to achieve fully passive, bias-free non-reciprocal pulse routing in standard silicon photonic platforms, which is of special interest for chip-scale LiDAR. The system architecture was optimized by photonics inverse design. To increase the non-reciprocal intensity range while preserving high transmission, a cascaded system of Fano and Lorentzian resonators was studied. Quasi-unitary forward transmission as well as a broad operating power range were demonstrated to illustrate the achievement of the essential, but previously elusive, functionalities required for application of these passive non-reciprocal devices to practical photonic systems. Although such nonlinearity-based devices are mainly useful for pulsed or periodic source applications due to dynamic reciprocity constraints¹⁶, the non-reciprocal signal routing demonstrated in this work represents a critical advance towards many other practical applications of immediate interest in photonics—self-pulsing lasers³⁸, nonlinear pulse shaping^{39,40}, photonic analog-to-digital converters⁴¹ and all-optical switches⁴²—for advanced optical communications and signal processing, spectroscopy and all-optical circuits in a silicon-nanoelectronics-compatible photonic platform⁴³.

Online content

Any methods, additional references, Nature Research reporting summaries, source data, extended data, supplementary information, acknowledgements, peer review information; details of author contributions and competing interests; and statements of data and code availability are available at <https://doi.org/10.1038/s41566-020-0606-0>.

Received: 12 May 2019; Accepted: 13 February 2020;

Published online: 23 March 2020

References

1. Yu, Z. & Fan, S. Complete optical isolation created by indirect interband photonic transitions. *Nat. Photon.* **3**, 91–94 (2009).
2. Lira, H., Yu, Z., Fan, S. & Lipson, M. Electrically driven nonreciprocity induced by interband photonic transition on a silicon chip. *Phys. Rev. Lett.* **109**, 033901 (2012).
3. Sounas, D. L. & Alù, A. Non-reciprocal photonics based on time modulation. *Nat. Photon.* **11**, 774–783 (2017).
4. Bi, L. et al. On-chip optical isolation in monolithically integrated non-reciprocal optical resonators. *Nat. Photon.* **5**, 758–762 (2011).
5. Zhang, Y. et al. Monolithic integration of broadband optical isolators for polarization-diverse silicon photonics. *Optica* **6**, 473–478 (2019).
6. Huang, D. et al. Electrically driven and thermally tunable integrated optical isolators for silicon photonics. *IEEE J. Sel. Top. Quantum Electron.* **22**, 271–278 (2016).
7. Sohn, D. B., Kim, S. & Bahl, G. Time-reversal symmetry breaking with acoustic pumping of nanophotonic circuits. *Nat. Photon.* **12**, 91–97 (2018).
8. Kittlaus, E. A., Otterstrom, N. T., Kharel, P., Gertler, S. & Rakich, P. T. Non-reciprocal interband Brillouin modulation. *Nat. Photon.* **12**, 613–619 (2018).
9. Gallo, K., Assanto, G., Parameswaran, K. R. & Fejer, M. M. All-optical diode in a periodically poled lithium niobate waveguide. *Appl. Phys. Lett.* **79**, 314–316 (2001).
10. Fan, L. et al. An all-silicon passive optical diode. *Science* **335**, 447–450 (2012).
11. Mahmoud, A. M., Davoyan, A. R. & Engheta, N. All-passive nonreciprocal metasurface. *Nat. Commun.* **6**, 8359 (2015).
12. Yu, Y. et al. Nonreciprocal transmission in a nonlinear photonic-crystal fano structure with broken symmetry. *Laser Photon. Rev.* **9**, 241–247 (2015).
13. Peng, B. et al. Parity-time-symmetric whispering-gallery microcavities. *Nat. Phys.* **10**, 394–398 (2014).
14. Chang, L. et al. Parity-time symmetry and variable optical isolation in active-passive-coupled microresonators. *Nat. Photon.* **8**, 524–529 (2014).
15. Del Bino, L. et al. Microresonator isolators and circulators based on the intrinsic nonreciprocity of the Kerr effect. *Optica* **5**, 279–282 (2018).
16. Shi, Y., Yu, Z. & Fan, S. Limitations of nonlinear optical isolators due to dynamic reciprocity. *Nat. Photon.* **9**, 388–392 (2015).
17. Komlenovic, T. et al. Photonic integrated circuits using heterogeneous integration on silicon. *Proc. IEEE* **106**, 2246–2257 (2018).
18. Fan, L. et al. Silicon optical diode with 40 dB nonreciprocal transmission. *Opt. Lett.* **38**, 1259–1261 (2013).
19. Kim, J., Kim, S. & Bahl, G. Complete linear optical isolation at the microscale with ultralow loss. *Sci. Rep.* **7**, 1647 (2017).
20. Trocha, P. et al. Ultrafast optical ranging using microresonator soliton frequency combs. *Science* **359**, 887–891 (2018).
21. Sounas, D. L. & Alù, A. Fundamental bounds on the operation of Fano nonlinear isolators. *Phys. Rev. B* **97**, 115431 (2018).
22. Sounas, D. L., Soric, J. & Alù, A. Broadband passive isolators based on coupled nonlinear resonances. *Nat. Electron.* **1**, 113–119 (2018).
23. Piggott, A. Y. et al. Inverse design and demonstration of a compact and broadband on-chip wavelength demultiplexer. *Nat. Photon.* **9**, 374–377 (2015).
24. Piggott, A. Y., Petykiewicz, J., Su, L. & Vučković, J. Fabrication-constrained nanophotonic inverse design. *Sci. Rep.* **7**, 1786 (2017).
25. Fano, U. Effects of configuration interaction on intensities and phase shifts. *Phys. Rev.* **124**, 1866–1878 (1961).
26. Fan, S., Suh, W. & Joannopoulos, J. D. Temporal coupled-mode theory for the Fano resonance in optical resonators. *J. Opt. Soc. Am. A* **20**, 569–572 (2003).
27. Fischer, K. A. et al. On-chip architecture for self-homodyned nonclassical light. *Phys. Rev. Appl.* **7**, 044002 (2017).
28. Yu, Y. et al. Fano resonance control in a photonic crystal structure and its application to ultrafast switching. *Appl. Phys. Lett.* **105**, 061117 (2014).
29. Wang, K. X., Yu, Z., Sandhu, S. & Fan, S. Fundamental bounds on decay rates in asymmetric single-mode optical resonators. *Opt. Lett.* **38**, 100–102 (2013).
30. Salem, R. et al. Signal regeneration using low-power four-wave mixing on silicon chip. *Nat. Photon.* **2**, 35–38 (2008).
31. Slavík, R. et al. All-optical phase and amplitude regenerator for next-generation telecommunications systems. *Nat. Photon.* **4**, 690–695 (2010).
32. Li, L. et al. All-optical regenerator of multi-channel signals. *Nat. Commun.* **8**, 884 (2017).
33. Sun, J., Timurdogan, E., Yaacobi, A., Hosseini, E. S. & Watts, M. R. Large-scale nanophotonic phased array. *Nature* **493**, 195–199 (2013).
34. Dietrich, P.-I. et al. In situ 3D nanoprinting of free-form coupling elements for hybrid photonic integration. *Nat. Photon.* **12**, 241–247 (2018).
35. Arbabí, A., Horie, Y., Ball, A. J., Bagheri, M. & Faraon, A. Subwavelength-thick lenses with high numerical apertures and large efficiency based on high-contrast transmittarrays. *Nat. Commun.* **6**, 7069 (2015).
36. Cheng, Q., Rumley, S., Bahadori, M. & Bergman, K. Photonic switching in high performance datacenters. *Opt. Express* **26**, 16022–16043 (2018).
37. Hadad, Y., Soric, J. C., Khanikaev, A. B. & Alù, A. Self-induced topological protection in nonlinear circuit arrays. *Nat. Electron.* **1**, 178–182 (2018).
38. Yu, Y., Xue, W., Semenova, E., Yvind, K. & Mork, J. Demonstration of a self-pulsing photonic crystal Fano laser. *Nat. Photon.* **11**, 81–84 (2017).
39. Bekele, D. A. et al. Pulse carving using nanocavity-enhanced nonlinear effects in photonic crystal Fano structures. *Opt. Lett.* **43**, 955–958 (2018).
40. Bekele, D. A. et al. Signal reshaping and noise suppression using photonic crystal Fano structures. *Opt. Express* **26**, 19596–19605 (2018).
41. Li, P. et al. All-optical analog comparator. *Sci. Rep.* **6**, 31903 (2016).
42. Dong, G., Wang, Y. & Zhang, X. High-contrast and low-power all-optical switch using Fano resonance based on a silicon nanobeam cavity. *Opt. Lett.* **43**, 5977–5980 (2018).
43. Atabaki, A. H. et al. Integrating photonics with silicon nanoelectronics for the next generation of systems on a chip. *Nature* **556**, 349–354 (2018).
44. Tamura, K., Ippen, E., Haus, H. & Nelson, L. 77-fs pulse generation from a stretched-pulse mode-locked all-fiber ring laser. *Opt. Lett.* **18**, 1080–1082 (1993).

Publisher's note Springer Nature remains neutral with regard to jurisdictional claims in published maps and institutional affiliations.

© The Author(s), under exclusive licence to Springer Nature Limited 2020

Methods

Inverse design. Stanford Photonics Inverse Design Software (SPINS)^{45,46}, based on the previously described fabrication-constrained inverse design methodology^{23,24}, was used to inverse design waveguide reflectors for target reflections of 60, 80 and 99% for 1,550 nm fundamental-mode TE-polarized light. These reflectors were designed inside the 500 nm-wide input waveguide with a design area of $500 \times 2,000 \text{ nm}^2$ and a minimum feature size constraint of 120 nm. More inverse design details are provided in Supplementary Section IV.

Characterization. Transmission measurements of the non-reciprocal devices were performed by coupling a c.w. laser through a single-mode fibre onto the chip via grating couplers⁴⁷ and monitoring the transmitted power through the waveguide-coupled device in the forward and backward directions while sweeping the laser input power (measurement wavelengths: 1,541.4 nm in Fig. 1; 1,533.87 in Fig. 2; 1,533.87, 1,541.4, 1,547.5, 1,552.1, 1,556.6 and 1,562 nm in Fig. 3b; 1,562 nm in panels 1, 3 and 4 of Fig. 3c; 1,547.5 nm in panel 2 of Fig. 3c). The transmission values were normalized by performing a transmission measurement of a single waveguide with grating couplers. The transmission was recorded over a spectral span of 250 GHz with a frequency increment of $\sim 200 \text{ MHz}$. The laser frequency was calibrated using fibre interferometer⁴⁸ and the grating coupling efficiency showed $\pm 0.25 \text{ dB}$ variations over 10 devices on the same chip. We measured the transmission of 10 waveguides with grating couplers and used the average of the transmission spectra for the normalization. The propagation direction was changed by implementing a fibre switch. It is important to note that the transmissions in both directions were measured without counter-propagating waves in the device.

Resonator design parameters. The resonator design parameters are as follows: waveguide–cavity gap = 200 nm, cavity–waveguide interaction length = 18.3 μm , PTE offset relative to the midplane of a single Fano resonator = 2.28 μm , delay lengths between Fano and Lorentzian resonators = 44 and 43.75 μm in panels 3 and 4 of Fig. 3c, respectively.

Data availability

The data that support the plots within this paper and other findings of this study are available from the corresponding author upon reasonable request.

References

45. Vuckovic, J. et al. Inverse design software for nanophotonic structures — spins. *Stanford University* http://techfinder.stanford.edu/technologies/S18-012_inverse (2018).
46. Su, L. et al. Nanophotonic inverse design with SPINS: software architecture and practical considerations. *Appl. Phys. Rev.* <https://doi.org/10.1063/1.5131263> (2020).
47. Sapra, N. V. et al. Inverse design and demonstration of broadband grating couplers. *IEEE J. Sel. Top. Quantum Electron.* **25**, 1–7 (2019).
48. Yang, K. Y. et al. Bridging ultrahigh-Q devices and photonic circuits. *Nat. Photon.* **12**, 297–302 (2018).

Acknowledgements

We acknowledge insightful discussions with D. Sounas, W. Bogaerts, D. A. B. Miller, P. Del'Haye, M. Soltani, L. Chang and J. E. Bowers, and are also grateful for technical advice from C. Langrock, B. Buscaino, N. V. Sapra, L. Su and J. M. Kahn. The silicon devices were fabricated in the Stanford Nanofabrication Facility and the Stanford Nano Shared Facilities. K.Y.Y. acknowledges support from a Quantum and Nano Science and Engineering postdoctoral fellowship. J.S. acknowledges support from the National Science Foundation Graduate Research Fellowship (grant no. DGE-1656518) and M.C. is supported by a Rubicon postdoctoral fellowship by The Netherlands Organization for Scientific Research (NWO). This work is funded by the Air Force Office of Scientific Research under the AFOSR MURI programme (award no. FA9550-17-1-0002) and the Gordon and Betty Moore Foundation (GBMF4744 and GBMF4743). We thank G. Pomrenke and the AFOSR MURI programme management team for discussions throughout the project.

Author contributions

K.Y.Y., J.S., M.C., A.Alù and J.V. conceived the experiments. K.Y.Y., J.S. and M.C. designed the device. K.Y.Y. and J.S. fabricated and tested the devices with assistance from M.C., A.D., G.H.A., M.S. and D.V. M.C. and K.Y.Y. conducted numerical simulations. K.Y.Y. and A.D. conducted optical ranging measurement with assistance from J.S., M.C. and D.V. All authors analysed the data and contributed to writing the manuscript. J.V. and A.Alù supervised the project.

Competing interests

The authors declare no competing interests.

Additional information

Supplementary information is available for this paper at <https://doi.org/10.1038/s41566-020-0606-0>.

Correspondence and requests for materials should be addressed to J.V.

Reprints and permissions information is available at www.nature.com/reprints.